

# AN IMMERSED BOUNDARY MODEL OF THE COCHLEA WITH PARAMETRIC FORCING

WILLIAM KO<sup>†</sup> AND JOHN M. STOCKIE<sup>†</sup>

**Abstract.** The cochlea or inner ear has a remarkable ability to amplify sound signals. This is understood to derive at least in part from some active process that magnifies vibrations of the basilar membrane (BM) and the cochlear partition in which it is embedded, to the extent that it overcomes the effect of viscous damping from the surrounding cochlear fluid. Many authors have associated this amplification ability to some type of mechanical resonance within the cochlea, however there is still no consensus regarding the precise cause of amplification. Our work is inspired by experiments showing that the outer hair cells within the cochlear partition change their lengths when stimulated, which can in turn cause periodic distortions of the BM and other structures in the cochlea. This paper investigates a novel fluid-mechanical resonance mechanism that derives from hydrodynamic interactions between an oscillating BM and the surrounding cochlear fluid. We present a model of the cochlea based on the immersed boundary method, in which a small-amplitude periodic internal forcing due to outer hair cells can induce parametric resonance. A Floquet stability analysis of the linearized equations demonstrates the existence of resonant (unstable) solutions within the range of physical parameters corresponding to the human auditory system. Numerical simulations of the immersed boundary equations support the analytical results and clearly demonstrate the existence of resonant solution modes. These results are then used to illustrate the influence of parametric resonance on wave propagation along the BM and explicit comparisons are drawn with results from another two-dimensional cochlea model.

**Key words.** cochlea, basilar membrane, immersed boundary method, fluid-structure interaction, parametric resonance.

**AMS subject classifications.** 35B34, 74F10, 76D05, 76Z05

**1. Introduction.** The cochlea or inner ear is a fluid-filled, spiral-wound cavity that is the central source of frequency selectivity in the hearing system of humans and many other animals. The cochlea is divided on its primary axis into two main fluid chambers, the scala tympani and scala vestibuli, by a structure known as the cochlear partition (CP). The CP itself consists of an elastic membrane known as the basilar membrane (BM), on top of which is mounted the organ of Corti containing the mechanosensitive hair cells that are the primary sensory receptors in the ear. Figure 1.1 contains a picture of an unwound cochlea with a simplified view of the CP showing only the BM. Sound vibrations entering the outer ear are transferred to the cochlear duct and BM by the stapes, and then propagate from base to apex along the BM and the surrounding fluid. The BM has a fine frequency tuning ability that distinguishes between different frequencies by localizing the peak amplitude of incident travelling waves. This “place theory” was developed and validated experimentally by von Békésy [54] and shows that the peak location is closer to the base for high frequencies and to the apex for low frequencies, as illustrated in Figure 1.1.

A second defining feature of the cochlea, which sets it apart from other sensory receptors, is its ability to amplify extremely weak sound signals that would otherwise be immediately damped out due to viscous dissipation in the cochlear fluid. Many authors have attributed this amplification ability to some active process related to resonance, which experiments have connected with mechanical properties of various structures making up the CP [11, 13, 19, 20, 42]. In particular, the outer hair cells in the organ of Corti are stimulated by BM deflections caused by pressure waves travelling through the cochlear fluid. The hair cell stimulation leads to either *somatic motility*, wherein the hair cell changes its length in response to electrical signals induced when the hair bundle on its tip is deflected; or *active hair bundle motility* in which the hair bundle itself generates additional forces that initiate a shearing action between the BM and the overlying tectorial membrane. Both of these effects are believed to contribute to the cochlear active process, but there is still no consensus in the literature regarding the precise cause of amplification [3, 50].

---

<sup>†</sup>Department of Mathematics, Simon Fraser University, 8888 University Drive, Burnaby, BC, V5A 1S6, Canada (wka11@sfu.ca, jstockie@sfu.ca).

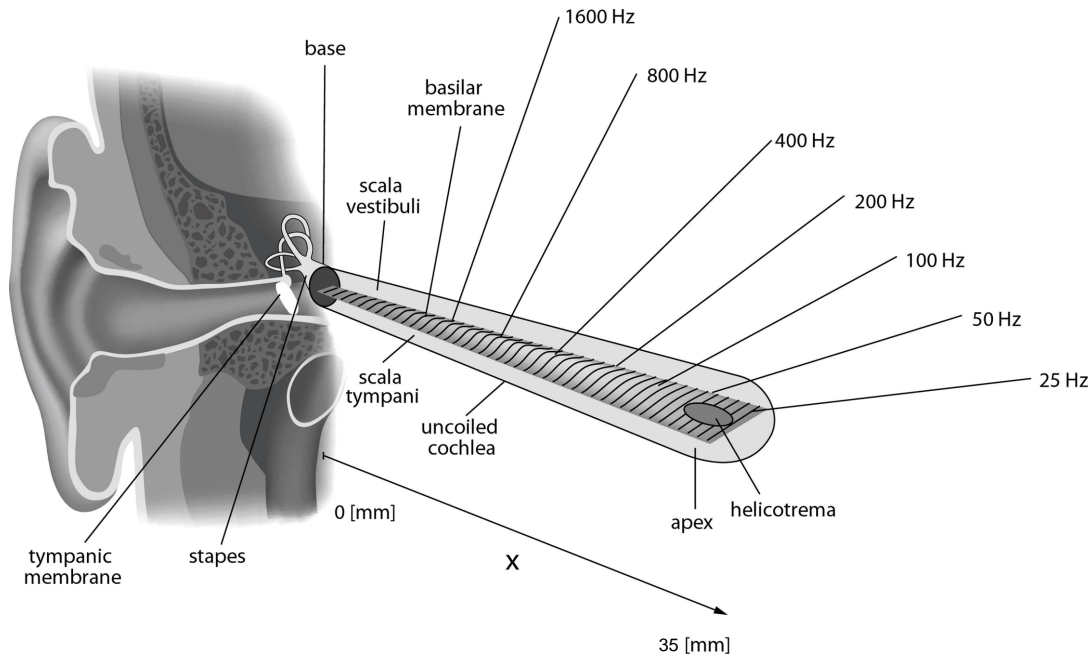


FIG. 1.1. Diagram of an uncoiled cochlea and BM, showing the relative location of maximal BM response for several sound frequencies in the human audible range. This is a simplified view of the cochlear partition, depicting only the BM and omitting other structural components such as the organ of Corti, outer hair cells, and tectorial membrane. Source: [25, Fig. 2] (distributed under the Creative Commons License).

Many mathematical and computational models of the cochlea have appeared since the seminal work of von Békésy [54]. The earliest two-dimensional models of the cochlea describe the BM as a collection of damped mass-spring systems and also reduce the fluid dynamics to a simple linear potential flow [1, 29, 40]. The spring constant decreases exponentially along the BM from base to apex, which coincides with BM stiffness values measured in experiments [54]. The BM is treated as a passive structure to which is applied a sinusoidal external forcing term that mimics the input of sound energy from the stapes. These models give predictions of BM dynamics that agree qualitatively with the behaviours observed by von Békésy. Inselberg and Chadwick [21] proposed a similar model in which the BM is represented as an Euler-Bernoulli beam, and showed not only that the place principle still holds but also that fluid viscosity is required to obtain travelling wave solutions along the BM as opposed to simply standing waves [7]. Pozrikidis [47] revisited this last approach by replacing the sinusoidal stapes motion with a point source at the stapes position and a point sink at the round window, and then solving the resulting equations using a boundary integral method. Another noteworthy class of models based on transmission line equations was introduced in the pioneering work of Zweig [56] and de Boer [12] and has since been applied in many more recent studies such as [14, 53].

To obtain a more realistic model of the fluid dynamics in the cochlea as well as the hydrodynamic interactions between the fluid and BM, several authors have exploited the immersed boundary (or IB) method. The IB method was originally developed by Peskin to simulate blood flow in the beating heart [45] and has since been applied to many problems in biofluid dynamics, including the cochlea. LeVeque et al. [30, 31] employed an IB model in which the fluid obeys the linearized Stokes equations and the elasticity of the cochlea is treated using simple elastic springs. They derived an asymptotic solution for travelling waves along the BM, from which they drew conclusions regarding the effects of fluid viscosity on these waves. Beyer and LeVeque [4] performed numerical simulations of a related IB model, with the primary difference being that their fluid obeys the full (nonlinear) Navier-Stokes equations. All of the aforementioned immersed boundary models approximate the geometry of the cochlea and BM by a straight (uncoiled) configuration. Although the curvature of the cochlear duct has a relatively small influence on the fluid dynamics [16], there is nonetheless some evidence to suggest that within the most tightly coiled apical region of the BM that is

stimulated by the lowest frequency sounds, curvature cannot be ignored [34]. To this end, a much more detailed IB model capturing the full 3D geometry of the cochlea was developed in [17] that reproduced important features of BM dynamics.

The goal of this paper is to use the IB method to investigate possible resonant phenomena that contribute to mechanical amplification of basilar membrane oscillations in the cochlea. Our study is inspired by three main observations: first, direct experimental evidence that outer hair cells embedded within the organ of Corti in the CP undergo periodic contractions when the ear is stimulated by sound waves [20, 23, 36]; second, the suggestion by several authors that these hair cell contractions can in turn modulate the stiffness in the BM [32, 35, 41] which we take as an assumption; and third, the analytical results of Cortez et al. [10] that uncovered parametric instabilities arising from the fluid-structure interaction in internally-forced immersed boundaries with a time-varying stiffness parameter. Taken together, these three observations suggest that there is merit in investigating the hypothesis that internal forcing in the basilar membrane due to sound stimulation can engender parametric resonance in an IB model of the cochlea.

One of the main contributions of this work is to extend the previous parametric resonance analysis for an elastic membrane with a periodically-varying stiffness parameter [10] to the case where stiffness depends on both time and space. Our results may also contribute new insights into the understanding of fine-frequency tuning and amplification in the cochlea since many previous cochlea models (described above) treat the outer hair cell contractions as an external forcing, over-simplify the fluid mechanics, and/or ignore the fluid-structure interaction. For example, it is common for papers to question the ability of linked mechanical oscillator models to capture cochlear amplification by arguing that damping due to viscosity of the cochlear fluid is simply too large [19]. This argument is valid if the active process driving the cochlea appears as an external forcing in the model, but not when the force acts internally through a parameter – in the latter case, parametric resonance can occur in which large amplitude oscillations (unbounded in the idealized linear case) arise even in the presence of damping [8]. Finally, we draw a distinction between our approach and other models incorporating resonance effects that act *locally*, such as the transmission line models based on coupled mechanical oscillators where each line element resonates individually. In contrast, our model exhibits *global resonance* owing to the non-local nature of the coupling between the BM and the surrounding fluid.

**2. Mathematical Model.** Following the IB cochlea model derived by Peskin in [44] and developed in more detail in [31], we consider a simple 2D geometry pictured in Figure 2.1 in which the cochlear duct of length  $L$  is treated as a rectangular strip  $\Omega = [0, L] \times \mathbb{R}$ , along the center of which lies the BM. This work is primarily concerned with the effects of parametric forcing on BM

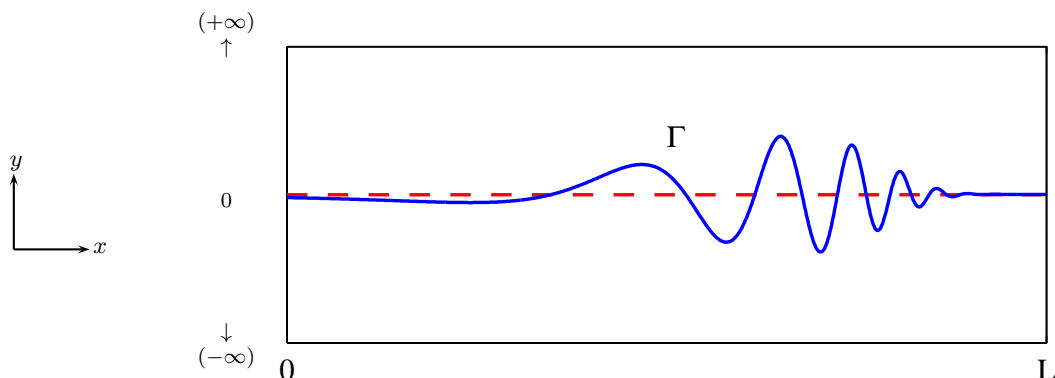


FIG. 2.1. *Geometry of the 2D immersed boundary model for the cochlea. The deformed BM is represented by a solid blue line  $\Gamma$ , and the flat equilibrium state by a red dotted line. To simplify the analysis, even symmetry is imposed across  $x = 0$  and  $x = L$  so that the solution is defined for all  $x \in \mathbb{R}$ , although only values of  $x \in [0, L]$  have physical relevance.*

oscillations and so we simplify the model by isolating the membrane from any boundary effects due to the cochlear walls. For the purposes of the mathematical analysis, we take the depth of the

cochlear duct to be infinite ( $y \rightarrow \pm\infty$ ) which is consistent with the *short-wave approximation* [51] and has been used previously by various authors [24, 30]. This assumption neglects effects such as coherent backscattering localized near the travelling wave peak [51], but we have found that this does not significantly impact on the results of our stability analysis. Furthermore, we impose Neumann boundary conditions in the  $x$ -direction which is an assumption that has also been justified for other cochlea models [40, 55].

The fluid in which the BM is immersed is governed by the incompressible Navier-Stokes equations

$$(2.1) \quad \rho \left( \frac{\partial \mathbf{u}}{\partial t} + \mathbf{u} \cdot \nabla \mathbf{u} \right) = -\nabla p + \mu \Delta \mathbf{u} + \mathbf{f},$$

$$(2.2) \quad \nabla \cdot \mathbf{u} = 0,$$

where  $\mathbf{u}(\mathbf{x}, t)$  is velocity,  $p(\mathbf{x}, t)$  is pressure,  $\rho$  is density, and  $\mu$  is viscosity. The elastic force exerted on the fluid by the membrane is given by

$$(2.3) \quad \mathbf{f}(\mathbf{x}, t) = \int_0^L K(s, t) (\mathbf{X}_0 - \mathbf{X}) \delta(\mathbf{x} - \mathbf{X}) ds,$$

where  $\delta(\mathbf{x})$  is the two-dimensional Dirac delta function,  $\mathbf{X}(s, t)$  is the position of the membrane parameterized by the Lagrangian coordinate  $s \in [0, L]$ , and  $\mathbf{X}_0(s) = (s, 0)$  is the horizontal equilibrium or rest state. This force can be thought of as arising from a membrane that is connected to its resting position via a series of Hookean springs with ‘‘spring constant’’ or stiffness  $K(s, t)$ . The elastic stiffness parameter is a function of time and space given by

$$(2.4) \quad K(s, t) = \sigma e^{-\lambda s} (1 + 2\tau \sin(\omega t)),$$

where  $\sigma$  is the time-averaged elastic stiffness constant (units of  $\text{g cm}^{-2} \text{s}^{-2}$ ) and  $\lambda$  captures the spatial variation in stiffness along the BM. The value of  $\lambda \approx 1.4 \text{ cm}^{-1}$  has been determined for a human cochlea experimentally by von Békésy [54] and others, based on the observation that the BM stiffness at the apex is approximately two orders of magnitude smaller than that at the base, and that it decays roughly exponentially. The time-dependent factor in the stiffness encapsulates the parametric forcing with amplitude  $\tau$  and frequency  $\omega$  arising from outer hair cells that contract/expand in response to BM oscillations [6, 18, 20]. Note in particular that the forcing frequency  $\omega$  is taken to be the same as that of the input sound signal and is also constant in space, which assumes that the outer hair cells contract in synchrony along the entire CP. This is in contrast with most other models of the cochlea that consider hair cell contractions in response to local stimuli, which would correspond to a stiffness parameter having spatiotemporal dependence that is not separable. There is nothing in our analytical approach that prevents us from considering this situation, but we nonetheless restrict our attention to the separable form in (2.4) for the sake of simplicity.

We close the system of equations with an expression for the membrane motion

$$(2.5) \quad \frac{\partial \mathbf{X}}{\partial t} = \mathbf{u}(\mathbf{X}, t) = \int_{\Omega} \mathbf{u}(\mathbf{x}, t) \delta(\mathbf{x} - \mathbf{X}) d\mathbf{x},$$

which is equivalent to the fluid no-slip condition along the immersed boundary.

To simplify the analysis in the remainder of this paper, we non-dimensionalize the problem by introducing the following scalings

$$(2.6) \quad \mathbf{x} = \frac{L\tilde{\mathbf{x}}}{\pi}, \quad t = \frac{\tilde{t}}{\omega}, \quad \mathbf{u} = U_c \tilde{\mathbf{u}}, \quad p = P_c \tilde{p}, \quad \mathbf{X} = \frac{L\tilde{\mathbf{X}}}{\pi}, \quad s = \frac{L\tilde{s}}{\pi},$$

where the tildes denote a non-dimensional quantity. The characteristic velocity and pressure scales,  $U_c$  and  $P_c$ , will be specified shortly. The horizontal extent of the rescaled domain  $\tilde{\Omega} = [0, \pi] \times \mathbb{R}$  is chosen for reasons of mathematical convenience, in order to eliminate a factor of  $\pi$  that would otherwise appear in the solutions derived in section 3.

Substituting the above variables into the governing equations (2.1)–(2.5) yields

$$(2.7) \quad \frac{\partial \tilde{\mathbf{u}}}{\partial t} + \tilde{\mathbf{u}} \cdot \tilde{\nabla} \tilde{\mathbf{u}} = -\tilde{\nabla} \tilde{p} + \nu \tilde{\Delta} \tilde{\mathbf{u}} + \tilde{\mathbf{f}},$$

$$(2.8) \quad \tilde{\nabla} \cdot \tilde{\mathbf{u}} = 0,$$

$$(2.9) \quad \tilde{\mathbf{f}}(\tilde{\mathbf{x}}, \tilde{t}) = \int_0^\pi \tilde{K}(\tilde{\mathbf{X}}_0 - \tilde{\mathbf{X}}) \tilde{\delta}(\tilde{\mathbf{x}} - \tilde{\mathbf{X}}) d\tilde{s},$$

$$(2.10) \quad \tilde{K}(\tilde{s}, \tilde{t}) = \kappa e^{-\alpha \tilde{s}} (1 + 2\tau \sin \tilde{t}),$$

$$(2.11) \quad \frac{\partial \tilde{\mathbf{X}}}{\partial t} = \tilde{\mathbf{u}}(\tilde{\mathbf{X}}, \tilde{t}).$$

The velocity and pressure scales are chosen as

$$(2.12) \quad U_c = \frac{L\omega}{\pi} \quad \text{and} \quad P_c = \frac{\rho\omega^2 L^2}{\pi^2},$$

to reduce the number of dimensionless parameters appearing in the equations to four, consisting of  $\tau$  plus the three new quantities

$$(2.13) \quad \nu = \frac{\mu\pi^2}{\rho L^2 \omega}, \quad \kappa = \frac{\sigma\pi}{\rho L \omega^2}, \quad \alpha = \frac{\lambda L}{\pi}.$$

From this point onwards, the tildes will be dropped.

We next proceed to linearize the governing equations for the purpose of making the analysis tractable. The typical vertical displacement of the BM is approximately  $10^{-6}$  cm which is six orders of magnitude smaller than its length of 3.5 cm [54]. This implies that the flow Reynolds number is very low, on the order of  $10^{-6}$  or less, and so nonlinear effects can be ignored. Assuming that there is negligible coupling in the membrane along the longitudinal ( $x$ ) direction, we only consider membrane displacements in the  $y$ -direction. Another major simplification is achieved by eliminating the delta functions and reformulating the problem in terms of jump conditions across the BM. To do so, we integrate the governing equations across the membrane at its linearized rest state  $y = 0$  [28], yielding the alternate system of equations

$$(2.14) \quad \frac{\partial \mathbf{u}}{\partial t} = -\nabla p + \nu \Delta \mathbf{u},$$

$$(2.15) \quad \nabla \cdot \mathbf{u} = 0,$$

away from the BM and

$$(2.16) \quad \llbracket p \rrbracket = -\kappa e^{-\alpha x} (1 + 2\tau \sin t) h(x, t),$$

$$(2.17) \quad u(x, 0, t) = 0,$$

$$(2.18) \quad v(x, 0, t) = \frac{\partial h}{\partial t},$$

across the membrane where  $h(x, t)$  represents the vertical membrane displacement,  $\llbracket p \rrbracket(x, t) = p(x, 0^+, t) - p(x, 0^-, t)$  is the jump in pressure across the membrane, and  $u(x, y, t)$  and  $v(x, y, t)$  are the horizontal and vertical components of the vector velocity  $\mathbf{u}$ . Eqs. (2.14)–(2.18) were studied analytically in [31] without the time-varying stiffness parameter (that is, with  $\tau = 0$ ).

**3. Floquet Analysis.** Owing to the presence of a time-varying parameter in the system, we invoke Floquet theory [8] to analyze the stability of perturbations of the membrane from its resting state. Floquet theory assumes a solution of the form

$$(3.1) \quad u(\mathbf{x}, t) = e^{\gamma t} P(\mathbf{x}, t),$$

where the function  $P(\mathbf{x}, t)$  is periodic in time with period  $2\pi$ . The Floquet exponent  $\gamma \in \mathbb{C}$  determines the stability of the solution as  $t \rightarrow \infty$ . For the purposes of our analysis, we extend the

$x$ -domain to  $[-\pi, \pi]$  and impose even symmetry across  $x = 0$ . We then take the unknown variables to be of the form

$$(3.2) \quad u(x, y, t) = e^{\gamma t} \sum_{n=-\infty}^{\infty} \sum_{k=-\infty}^{\infty} u_k^n(y) e^{int} e^{ikx},$$

$$(3.3) \quad v(x, y, t) = e^{\gamma t} \sum_{n=-\infty}^{\infty} \sum_{k=-\infty}^{\infty} v_k^n(y) e^{int} e^{ikx},$$

$$(3.4) \quad p(x, y, t) = e^{\gamma t} \sum_{n=-\infty}^{\infty} \sum_{k=-\infty}^{\infty} p_k^n(y) e^{int} e^{ikx},$$

$$(3.5) \quad h(x, t) = e^{\gamma t} \sum_{n=-\infty}^{\infty} \sum_{k=-\infty}^{\infty} h_k^n e^{int} e^{ikx},$$

where we have assumed that  $P(\mathbf{x}, t)$  can be expanded using a Fourier series in both space and time. Our solution approach is similar to that used by Cortez et al. [10] (modulo the corrections in [27]) who analyzed the stability of a 2D circular membrane in response to a perturbation in the form of a single Fourier mode. In contrast, here we must represent each solution mode as an infinite Fourier series because of the mode-coupling through the spatial non-uniformity in the stiffness parameter which will be shown later in this section.

We begin by finding solutions for the  $y$ -dependent Fourier coefficients  $u_k^n$ ,  $v_k^n$  and  $p_k^n$ . Take the divergence of the momentum equations (2.14) and apply the incompressibility condition (2.15) to arrive at a Poisson problem for pressure

$$(3.6) \quad \Delta p = \sum_{n, k=-\infty}^{\infty} (-k^2 p_k^n(y) + p_k^{n''}(y)) \mathcal{E}_k^n = 0.$$

Here we have simplified notation by setting  $\mathcal{E}_k^n(x, t) = \exp[(\gamma + in)t + ikx]$  and denoting  $y$ -derivatives using primes. The  $\mathcal{E}_k^n$  are all linearly independent and so we have a decoupled system of ordinary differential equations for the  $p_k^n(y)$

$$(3.7) \quad -k^2 p_k^n(y) + p_k^{n''}(y) = 0 \quad \forall n, k \in \mathbb{Z},$$

which after imposing boundedness in  $y$  yields the pressure solution

$$(3.8) \quad p_k^n(y) = \begin{cases} a_k^n e^{ky} & \text{if } y < 0, \\ b_k^n e^{-ky} & \text{if } y > 0, \end{cases}$$

for each  $n, k \in \mathbb{Z}$ , with constants  $a_k^n$  and  $b_k^n$  yet to be determined. Note that taking  $k = 0$  is valid in the above expression since this implies simply a constant pressure in each sub-domain.

We can now solve for the Fourier coefficients of the vertical velocity component  $v$  by substituting the series (3.3) into the momentum equation to obtain

$$(3.9) \quad \sum_{n, k=-\infty}^{\infty} (\gamma + in) v_k^n(y) \mathcal{E}_k^n = \sum_{n, k=-\infty}^{\infty} (-p_k^{n'}(y) - \nu k^2 v_k^n(y) + \nu v_k^{n''}(y)) \mathcal{E}_k^n.$$

This is equivalent to the infinite linear system of ordinary differential equations

$$(3.10) \quad v_k^{n''}(y) - (\beta_k^n)^2 v_k^n(y) = \frac{1}{\nu} p_k^{n'}(y) \quad \forall n, k \in \mathbb{Z},$$

where

$$(3.11) \quad \beta_k^n = \sqrt{\frac{\gamma + in}{\nu} + k^2} \quad \text{with } \text{Re}\{\beta_k^n\} > 0.$$

Assuming that  $\gamma + in \neq 0$  and  $k \neq 0$ , the solution is

$$(3.12) \quad v_k^n(y) = \frac{1}{2\nu\beta_k^n} \begin{cases} -\frac{2k\beta_k^n}{(\beta_k^n)^2 - k^2} a_k^n e^{ky} + \left( \frac{k}{\beta_k^n - k} a_k^n + \frac{k}{\beta_k^n + k} b_k^n \right) e^{\beta_k^n y}, & \text{if } y < 0, \\ \frac{2\beta_k^n}{(\beta_k^n)^2 - k^2} b_k^n e^{-ky} - \left( \frac{k}{\beta_k^n - k} b_k^n + \frac{k}{\beta_k^n + k} a_k^n \right) e^{-\beta_k^n y}, & \text{if } y > 0. \end{cases}$$

The continuity equation reduces to

$$(3.13) \quad iku_k^n(y) + v_k^{n'}(y) = 0 \quad \forall n, k \in \mathbb{Z},$$

from which  $u_k^n(y)$  are found to be

$$(3.14) \quad u_k^n(y) = \frac{-i}{2k\nu} \begin{cases} -\frac{2k^2}{(\beta_k^n)^2 - k^2} a_k^n e^{ky} + \left( \frac{k}{\beta_k^n - k} a_k^n + \frac{k}{\beta_k^n + k} b_k^n \right) e^{\beta_k^n y}, & \text{if } y < 0, \\ -\frac{2k}{(\beta_k^n)^2 - k^2} b_k^n e^{-ky} + \left( \frac{k}{\beta_k^n - k} b_k^n + \frac{k}{\beta_k^n + k} a_k^n \right) e^{-\beta_k^n y}, & \text{if } y > 0. \end{cases}$$

We then impose the continuity conditions on velocity across the membrane

$$(3.15) \quad u_k^n(0^+) = u_k^n(0^-) = \frac{i}{2\nu} \left( \frac{1}{\beta_k^n + k} a_k^n + \frac{1}{\beta_k^n + k} b_k^n \right) = 0,$$

$$(3.16) \quad v_k^n(0^+) = v_k^n(0^-) = \frac{1}{2\nu\beta_k^n} \left( \frac{-k}{\beta_k^n + k} a_k^n + \frac{k}{\beta_k^n + k} b_k^n \right) = (\gamma + in)h_k^n,$$

which can be solved in terms of the  $h_k^n$  as

$$(3.17) \quad a_k^n = -\nu(\gamma + in) \frac{\beta_k^n + k}{k} \beta_k^n h_k^n,$$

$$(3.18) \quad b_k^n = \nu(\gamma + in) \frac{\beta_k^n + k}{k} \beta_k^n h_k^n.$$

We note that the special cases  $\gamma + in = 0$  and  $k = 0$  both yield the trivial solution,  $a_k^n = b_k^n = 0$ .

Using the jump condition (2.16), we can now formulate an infinite system of linear equations that connects all of the membrane coefficients,  $h_k^n$ . Substituting the solution for pressure into (2.16), we obtain

$$(3.19) \quad \sum_{n,k=-\infty}^{\infty} 2\nu(\gamma + in) \frac{\beta_k^n + k}{k} \beta_k^n h_k^n \mathcal{E}_k^n = \sum_{n,k=-\infty}^{\infty} -\kappa e^{-\alpha x} (1 + 2\tau \sin t) h_k^n \mathcal{E}_k^n,$$

provided that  $\gamma + in \neq 0$  and  $k \neq 0$ . In the special cases when  $\gamma + in = 0$  or  $k = 0$ , these equations reduce to

$$(3.20) \quad 0 = \sum_{n,k=-\infty}^{\infty} -\kappa e^{-\alpha x} (1 + 2\tau \sin t) h_k^n \mathcal{E}_k^n.$$

In order to proceed any further, we first need to expand the exponential ( $e^{-\alpha x}$ ) and sinusoidal ( $\sin t$ ) terms in their respective Fourier series. For the time-dependent factor, we can write  $1 + 2\tau \sin t = 1 - i\tau e^{it} + i\tau e^{-it}$ , but the Fourier series for the exponential function does not converge uniformly because  $e^{-\alpha x}$  is not a periodic function on  $[0, \pi]$ . It is for this reason that we have extended the spatial domain to  $[-\pi, \pi]$ , and then we simply need to remember that is only the portion with  $x \geq 0$  that is of physical interest. We instead use the even periodic extension  $e^{-\alpha|x|}$  of the elastic stiffness function on this extended interval. Then, for  $\gamma + in \neq 0$  and  $k \neq 0$  we have

$$(3.21) \quad \begin{aligned} & \sum_{n,k=-\infty}^{\infty} 2\nu(\gamma + in) \frac{\beta_k^n + k}{k} \beta_k^n h_k^n \mathcal{E}_k^n \\ &= \sum_{n,k=-\infty}^{\infty} -\kappa \left( \sum_{j=-\infty}^{\infty} c_j e^{ijx} \right) (1 - i\tau e^{it} + i\tau e^{-it}) h_k^n \mathcal{E}_k^n, \end{aligned}$$

while for  $\gamma + in = 0$  or  $k = 0$ ,

$$(3.22) \quad 0 = \sum_{n,k=-\infty}^{\infty} -\kappa \left( \sum_{j=-\infty}^{\infty} c_j e^{ijx} \right) (1 - i\tau e^{it} + i\tau e^{-it}) h_k^n \mathcal{E}_k^n,$$

where

$$(3.23) \quad c_j = \alpha \frac{1 - (-1)^j e^{-\alpha\pi}}{\pi(\alpha^2 + j^2)}$$

are the Fourier coefficients of  $e^{-\alpha|x|}$  on  $[-\pi, \pi]$ . The complex exponential terms involving  $x$  and  $t$  in Eqs. (3.21) and (3.22) introduce a shift in the indices of  $\mathcal{E}_k^n$  in both  $n$  and  $k$ , which has the effect of coupling the corresponding modes. We can then rearrange the sum in order to gather together all terms involving the common expression  $\mathcal{E}_k^n$ , and hence obtain

$$(3.24) \quad \frac{2\nu^2}{\kappa} (\beta_k^n - k) (\beta_k^n + k)^2 \frac{\beta_k^n}{k} h_k^n + \sum_{j=-\infty}^{\infty} c_{k-j} h_j^n = i\tau \sum_{j=-\infty}^{\infty} c_{k-j} (h_j^{n-1} - h_j^{n+1}),$$

for  $\gamma + in \neq 0$  and  $k \neq 0$  and

$$(3.25) \quad \sum_{j=-\infty}^{\infty} c_{k-j} h_j^n = i\tau \sum_{j=-\infty}^{\infty} c_{k-j} (h_j^{n-1} - h_j^{n+1}),$$

for either of the special cases  $\gamma + in = 0$  or  $k = 0$ . These last two equations comprise an infinite linear system for the  $h_j^n$  in which the spatially-dependent stiffness introduces a simultaneous coupling between all spatial modes that is not present in the spatially-uniform ( $\alpha = 0$ ) case from [10].

Because we are interested in investigating the stability of the parametrically forced problem, and in particular finding the stability boundary in parameter space, we only have to look for periodic solutions of Eqs. (3.24)–(3.25) in the situation when  $\text{Re}\{\gamma\} = 0$ . Furthermore, there are only two distinct values of  $\gamma$  that are of actual interest for determining the stability boundary: the first corresponds to  $\gamma = 0$  and will be referred to as the *harmonic* case; and the second,  $\gamma = \frac{1}{2}i$ , is called the *subharmonic* case. To ensure that the solution  $h(x, t)$  is real-valued, we impose *reality conditions* for the Fourier coefficients that apply to both time and space indices. In general, the reality condition for a two-dimensional Fourier series is  $h_k^n = \bar{h}_{-k}^{-n}$  where the overbar denotes the complex conjugate. However, we have to consider the harmonic and subharmonic cases separately when applying the condition in the temporal modes. Furthermore, we want to ensure an even spatial symmetry in our solutions which leads to a decoupling in the reality condition. Consequently, the reality conditions that we impose are

$$(3.26) \quad h_{-k}^n = h_k^n,$$

$$(3.27) \quad h_k^{-n} = \begin{cases} \bar{h}_k^n, & \text{for the harmonic case } (\gamma = 0), \\ \bar{h}_k^{n-1}, & \text{for the subharmonic case } (\gamma = \frac{1}{2}i). \end{cases}$$

As a result, the reality conditions introduce a certain symmetry between the Fourier coefficients such that we only need to consider non-negative values of  $n$  and  $k$ .

These choices of harmonic and subharmonic values for  $\gamma$  can be justified as follows. The solution form (3.1) implies that

$$(3.28) \quad u(\mathbf{x}, t + 2\pi n) = e^{\gamma(t+2\pi n)} P(\mathbf{x}, t) = \xi^n u(\mathbf{x}, t),$$

for any positive integer  $n$  where  $\xi = e^{\gamma 2\pi}$  and  $t$  is fixed. As  $n \rightarrow \infty$  the long term behaviour of the solution depends the value of  $\xi$ . We conclude that solutions are stable if  $|\xi| < 1$  and unstable if  $|\xi| > 1$ , where the special values  $\xi = \pm 1$  correspond to periodic solutions that define the marginal stability boundaries separating stable and unstable solutions. If  $\gamma = 0$ , then  $\xi = 1$  and

$$(3.29) \quad u(\mathbf{x}, t + 2\pi) = u(\mathbf{x}, t),$$



which is the  $2\pi$ -periodic harmonic solution. If  $\gamma = \frac{1}{2}i$ , then  $\xi = -1$  and

$$(3.30) \quad u(\mathbf{x}, t + 2\pi) = -u(\mathbf{x}, t), \quad u(\mathbf{x}, t + 4\pi) = u(\mathbf{x}, t),$$

which is the period-doubling subharmonic solution. These same relationships hold for all of the dependent variables.

We are aware of no analytical method for determining solutions to the infinite system (3.24)–(3.27) explicitly, and so we truncate the system at values of  $n = 0, 1, \dots, N$  and  $k = 1, 2, \dots, M$  and then approximate the solutions numerically. For  $k = 0$ , we have that  $h_0^n = 0$  for each  $n$  and so there is no need to include them in the linear system. The truncated system of equations can therefore be represented as a matrix equation

$$(3.31) \quad A\vec{h} = \tau B\vec{h},$$

where

$$(3.32) \quad \vec{h} = [\dots, \operatorname{Re}(h_k^n), \operatorname{Im}(h_k^n), \operatorname{Re}(h_{k+1}^n), \operatorname{Im}(h_{k+1}^n), \dots]^T$$

is a vector of length  $2M(N+1)$  containing all unknown coefficients,  $A$  (and  $B$ ) are block diagonal (tridiagonal) matrices respectively, both of block dimension  $(N+1) \times (N+1)$  where each block is size  $2M \times 2M$ . The block diagonal matrix  $A$  can be expressed as  $A = \operatorname{diag}(A^0, A^1, \dots, A^N)$  where each block has the form

$$(3.33) \quad A^n = \begin{bmatrix} C_{1,1} + D_1^n & C_{1,2} & \dots & C_{1,M} \\ C_{2,1} & C_{2,2} + D_2^n & & C_{2,M} \\ \vdots & & \ddots & \vdots \\ C_{M,1} & C_{M,2} & \dots & C_{M,M} + D_M^n \end{bmatrix},$$

with

$$(3.34) \quad C_{k,j} = \begin{bmatrix} c_{k-j} + c_{k+j} & 0 \\ 0 & c_{k-j} + c_{k+j} \end{bmatrix},$$

$$(3.35) \quad D_k^n = \frac{2\nu^2}{\kappa k} \begin{bmatrix} \operatorname{Re}\{(\beta_k^n - k)(\beta_k^n + k)^2 \beta_k^n\} & -\operatorname{Im}\{(\beta_k^n - k)(\beta_k^n + k)^2 \beta_k^n\} \\ \operatorname{Im}\{(\beta_k^n - k)(\beta_k^n + k)^2 \beta_k^n\} & \operatorname{Re}\{(\beta_k^n - k)(\beta_k^n + k)^2 \beta_k^n\} \end{bmatrix}.$$

For the harmonic case,  $D_k^0$  is simply the  $2 \times 2$  zero matrix. The block tridiagonal matrix  $B$  has the form

$$(3.36) \quad B = \begin{bmatrix} \tilde{B} & \tilde{B} & & & \\ \hat{B} & 0 & -\hat{B} & & \\ & \ddots & \ddots & \ddots & \\ & & \hat{B} & 0 & -\hat{B} \\ & & & \hat{B} & 0 \end{bmatrix},$$

where

$$(3.37) \quad \hat{B} = \begin{bmatrix} \hat{C}_{1,1} & \hat{C}_{1,2} & \dots & \hat{C}_{1,M} \\ \hat{C}_{2,1} & \hat{C}_{2,2} & & \hat{C}_{2,M} \\ \vdots & & \ddots & \vdots \\ \hat{C}_{M,1} & \hat{C}_{M,2} & \dots & \hat{C}_{M,M} \end{bmatrix}, \quad \tilde{C}_{k,j} = \begin{bmatrix} 0 & -c_{k-j} - c_{k+j} \\ c_{k-j} + c_{k+j} & 0 \end{bmatrix}.$$

The reality conditions determine the first block row of  $B$ . For harmonic solutions,  $\tilde{B}$  is the  $2M \times 2M$  zero matrix while  $\hat{B}$  has the same form as  $\hat{B}$  in (3.37) except that the  $2 \times 2$  sub-blocks are

$$(3.38) \quad \tilde{C}_{k,j} = \begin{bmatrix} 0 & 2c_{k-j} + 2c_{k+j} \\ 0 & 0 \end{bmatrix}.$$

For subharmonic solutions  $\tilde{B} = -\hat{B}$ , and  $\check{B}$  consists of the  $2 \times 2$  sub-blocks

$$(3.39) \quad \check{C}_{k,j} = \begin{bmatrix} 0 & c_{k-j} + c_{k+j} \\ c_{k-j} + c_{k+j} & 0 \end{bmatrix}.$$

Now that the entries in the matrices  $A$  and  $B$  are all known, we can view (3.31) as an eigenvalue problem

$$(3.40) \quad A^{-1}B\vec{h} = \frac{1}{\tau}\vec{h},$$

where the key determinant of stability is the eigenvalue  $\frac{1}{\tau}$ . In particular, we are only concerned with those physically-relevant values of  $\tau$  that are real and are less than  $\frac{1}{2}$ , since this ensures that the elastic stiffness function  $K(s, t)$  is real and non-negative.

**4. Natural Modes for an Unforced Membrane.** Before solving the parametrically forced problem, we first examine the stability of the unforced membrane corresponding to  $\tau = 0$ . Previous stability analyses of the immersed boundary method showed that unforced membranes are always stable [10, 52] and we expect a similar result here. The Fourier coefficients of the unforced solution satisfy

$$(4.1) \quad \frac{2\phi\gamma}{k\nu} \sqrt{\frac{\gamma}{\nu} + k^2} \left( k + \sqrt{\frac{\gamma}{\nu} + k^2} \right) h_k^0 + \sum_{j=-\infty}^{\infty} c_{k-j} h_j^0 = 0$$

when  $k \neq 0$ , and

$$(4.2) \quad \sum_{j=-\infty}^{\infty} c_{k-j} h_j^0 = 0$$

when  $k = 0$ . We have introduced the new dimensionless parameter  $\phi = \nu^2/\kappa = \pi^3\mu^2/(\rho\sigma L^3)$ , which is a measure of the relative importance of viscous fluid force relative to elastic membrane force. The system of equations (4.1) and (4.2) can be written simply as a matrix system  $T\vec{h}^0 = \mathbf{0}$ , where the entries of the matrix  $T$  depend on the parameters  $\phi$ ,  $\gamma/\nu$  and  $\alpha$ . This linear system has non-trivial solutions only if  $\det(T) = 0$ , and so by fixing values of  $\phi$  and  $\alpha$  we can determine values of  $\gamma/\nu$  such that solutions to the homogeneous system exist. In practice, we proceed by first truncating the infinite series in (4.1) and in (4.2) to  $M$  terms, and then computing the determinant numerically.

Figure 4.1 depicts the zero contours of the real and imaginary parts of  $\det(T)$  for the specific choice of parameters  $\alpha = 1.56$  and  $M = 20$ , and two values of  $\phi = 5 \times 10^{-10}$ ,  $2 \times 10^{-4}$ . The points where the contours intersect correspond to the natural modes of the system. Observe that  $\text{Re}\{\gamma\}$  is always negative at the intersection points, from which we conclude that all solution modes are stable. We see next how the behaviour of the natural modes depends on  $\phi$ , the relative strength of fluid viscosity to membrane stiffness. For the relatively small value of  $\phi = 5 \times 10^{-10}$ , the dominant modes (which are slowest to decay) have non-zero  $\text{Im}\{\gamma\}$  and are therefore oscillatory. When  $\phi$  is increased to  $2 \times 10^{-4}$ , viscosity has a much stronger influence and the dominant (lowest wavenumber) modes decay without oscillations, although decaying oscillatory solutions still do exist. In both cases, the unforced modes always decay in time and hence any periodic or unstable solutions must arise from a periodic modulation of the membrane stiffness.

**5. Parametrically Forced Pure-Tone Response.** In this section, we demonstrate that an internally-forced membrane can generate travelling wave solutions that are similar to solutions obtained from other models that impose an external forcing. We compute harmonic solutions to (3.24)–(3.25) numerically and then choose the smallest physically-allowable value of  $\tau$  along with its corresponding eigenvector. We can reconstruct a periodic solution for  $h(x, t)$  using the series representation (3.5), which is then compared to the travelling wave solutions from [31] obtained when a pure-tone external forcing is applied. We take parameter values from [31] (listed in Table 5.1) that are also consistent with parameters reported elsewhere in the literature for the human

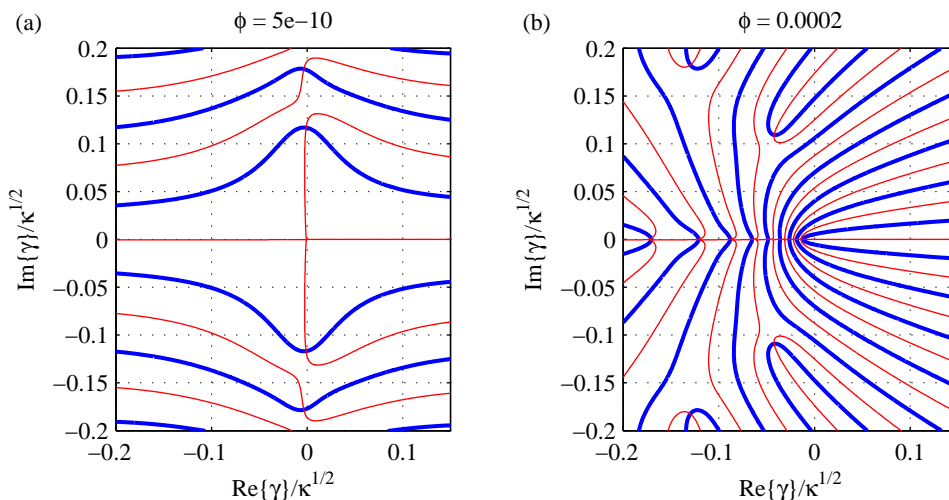


FIG. 4.1. Zero contours of the real (thick, blue) and imaginary parts (thin, red) of  $\det(T)$  for: (a)  $\phi = 5 \times 10^{-10}$  and (b)  $\phi = 2 \times 10^{-4}$ . In both cases, we take  $\alpha = 1.56$  and use  $M = 20$  modes. The resonant modes correspond to intersection points between the real and imaginary contours.

TABLE 5.1

Parameter values (or ranges) used in the cochlea simulations. Values are taken from [31] and (with the exception of  $\sigma$ ) correspond to the human cochlea.

<i>Physical parameters (cgs units):</i>	
fluid density	$\rho = 1.0 \text{ g cm}^{-3}$
fluid viscosity	$\mu = 0.02 \text{ g cm}^{-1} \text{ s}^{-1}$
elastic stiffness	$\sigma = 6 \times 10^5 \text{ g cm}^{-2} \text{ s}^{-2}$
elastic stiffness decay rate	$\lambda = 1.4 \text{ cm}^{-1}$
basilar membrane length	$L = 3.5 \text{ cm}$
forcing frequency	$\omega \in [400, 1600] \text{ s}^{-1}$
velocity scale	$U_c = \frac{\omega L}{\pi} \in [446, 1783] \text{ cm s}^{-1}$
pressure scale	$P_c = \frac{\rho \omega^2 L^2}{\pi^2} \in [2.0 \times 10^5, 3.2 \times 10^6] \text{ dyn cm}^{-2}$
<i>Dimensionless parameters:</i>	
dimensionless decay rate	$\alpha = 1.56$
forcing amplitude	$\tau \in [0, 0.5]$
dimensionless viscosity	$\nu \in [8.06 \times 10^{-6}, 1.61 \times 10^{-4}]$
dimensionless stiffness	$\kappa \in [0.135, 53.9]$
viscosity/stiffness ratio	$\phi = \frac{\nu^2}{\kappa} = \frac{\pi^3 \mu^2}{\rho \sigma L^3} = 4.8 \times 10^{-10}$

cochlea, with the only exception being the elastic stiffness value. Other cochlea models take values of  $\sigma$  that range from  $1 \times 10^7$  [29] to  $2 \times 10^9 \text{ g cm}^{-2} \text{ s}^{-2}$  [1]; however, we have chosen the smaller value of  $\sigma = 6 \times 10^5 \text{ g cm}^{-2} \text{ s}^{-2}$  for the purposes of this paper in order to permit a direct comparison with the results in [31] for a similar IB model.

Figure 5.1 shows solution profiles of the BM displacement curve  $h(x, t_{peak})$  for forcing frequencies  $\omega = 400, 800, 1200$  and  $1600 \text{ s}^{-1}$ , where  $t_{peak}$  represents the time when the maximum vertical BM displacement occurs. The wave envelope is determined by computing the absolute value of a complex-valued function whose real part is the BM profile and the imaginary part is its Hilbert transform [5, 26]. The envelope is normalized so that the maximum height is 1. These wave envelopes have the characteristic asymmetric shape seen in experiments [49], exhibiting an amplitude that increases gradually from base to peak, followed by a sharp decline at the apical end. The solid curve in each case corresponds to the harmonic mode for which the response frequency is equal to the forcing frequency. A qualitatively similar result is obtained for subharmonic solutions (dashed curves) except that the response occurs at a frequency equal to half that of the internal

forcing and so the wave profiles are shifted. This indicates that the location of the envelope peak depends on the response frequency and not the forcing frequency.

Through a combination of experiments and analysis, von Békésy showed [54] that the peak location of the travelling wave envelope actually depends logarithmically on the stimulus frequency. Figure 5.2 depicts the computed peak locations at various response frequencies, and our results lie nearly on a straight line which is consistent with the logarithmic dependence just mentioned. This plot also includes the asymptotic results derived from the model in [31] as a solid line, which is clearly very close to our own results. As a further validation, Figure 5.3 compares our BM displacement curve with the corresponding result from [31] for the frequency  $\omega = 400 \text{ s}^{-1}$ . Both profiles are shifted so that the wave envelope peak occurs at  $x = 0$ , after which we can see that the qualitative shape and solution envelope are quite similar. These numerical results demonstrate that external forcing is not required to obtain a realistic travelling wave solution on the BM, and indeed that parametric (internal) forcing in the BM stiffness can generate pure-tone solutions consistent with that observed in other models.

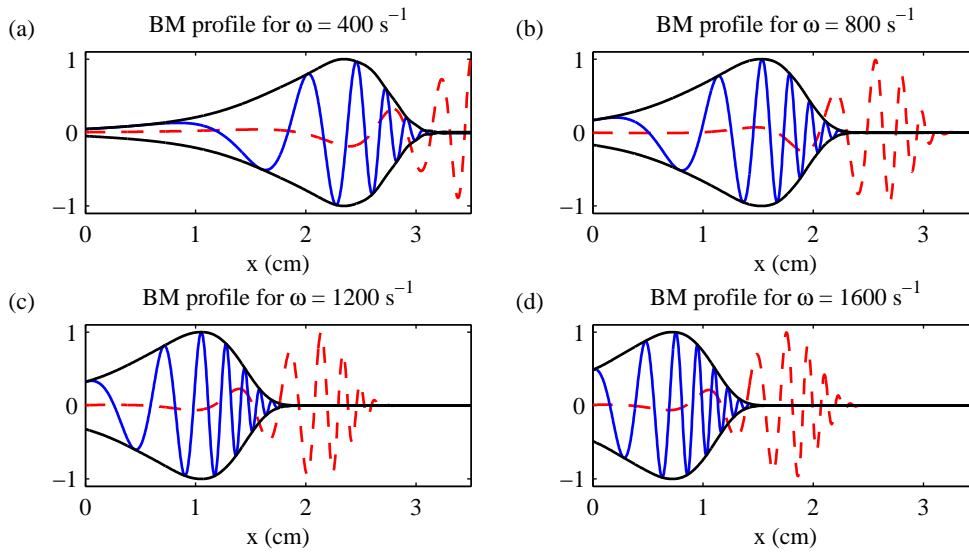


FIG. 5.1. Normalized BM displacement profiles for the harmonic (solid) and subharmonic (dashed) cases at frequencies  $\omega = 400, 800, 1200$  and  $1600 \text{ s}^{-1}$ .

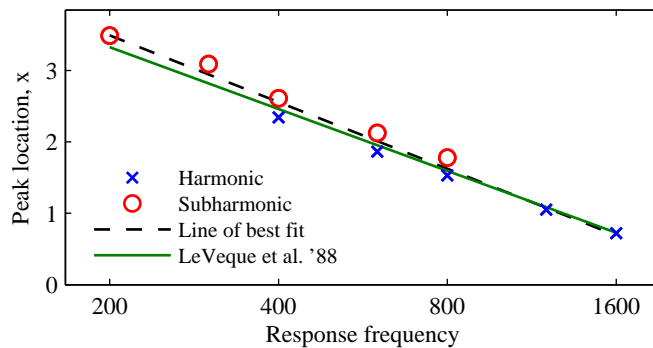


FIG. 5.2. BM envelope peak location plotted against response frequency, with the horizontal axis (frequency) plotted on a log scale. Harmonic (x) and subharmonic solutions (o) have response frequencies  $\omega$  and  $\omega/2$ , respectively.

## 6. Parametric Resonance.

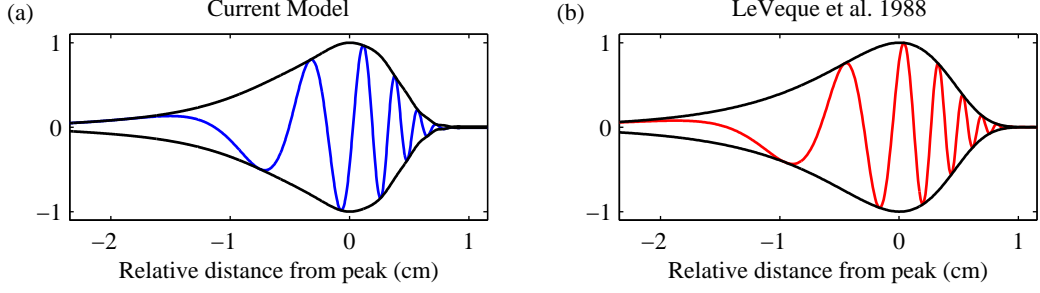


FIG. 5.3. Normalized BM displacement profiles from our IB model (left) and model by LeVeque et al. [31] (right) at a frequency of  $\omega = 400 \text{ s}^{-1}$ .

**6.1. Case  $\alpha = 0$ .** To gain more insight into solutions of the eigenvalue problem (3.40), we begin by considering the simple case  $\alpha = 0$  where the elastic stiffness does not depend on BM location and thus the spatial Fourier modes are decoupled. For each spatial wavenumber  $k$  we have

$$(6.1) \quad \frac{2\phi}{k}(\beta_k^n - k)(\beta_k^n + k)^2 \beta_k^n h_k^n + h_k^n = i\tau(h_k^{n-1} - h_k^{n+1})$$

for  $n = 0, 1, \dots, N$ . This equation may be rewritten in matrix form as

$$(6.2) \quad A_k \vec{h}_k = \tau B_k \vec{h}_k,$$

where for each value of  $k$

$$(6.3) \quad \vec{h}_k = [\text{Re}(h_k^0), \text{Im}(h_k^0), \dots, \text{Re}(h_k^N), \text{Im}(h_k^N)]^T,$$

$$(6.4) \quad A_k = \text{diag}(I + D_k^0, I + D_k^1, \dots, I + D_k^N),$$

$D_k^n$  is defined by (3.35) and  $I$  is the  $2 \times 2$  identity matrix. For the matrix  $B$ , we need to consider separately the two cases corresponding to harmonic solutions where

$$(6.5) \quad B_k = \begin{bmatrix} 0 & 0 & 0 & 2 & & & \\ 0 & 0 & 0 & 0 & & & \\ 0 & -1 & 0 & 0 & 0 & 1 & \\ 1 & 0 & 0 & 0 & -1 & 0 & \\ \hline & & 0 & -1 & 0 & 0 & 0 & 1 \\ & & 1 & 0 & 0 & 0 & -1 & 0 \\ \hline & & & & \ddots & & \ddots & \\ & & & & & & & \ddots \end{bmatrix},$$

and subharmonic solutions where

$$(6.6) \quad B_k = \begin{bmatrix} 0 & 1 & 0 & 1 & & & \\ 1 & 0 & -1 & 0 & & & \\ 0 & -1 & 0 & 0 & 0 & 1 & \\ 1 & 0 & 0 & 0 & -1 & 0 & \\ \hline & & 0 & -1 & 0 & 0 & 0 & 1 \\ & & 1 & 0 & 0 & 0 & -1 & 0 \\ \hline & & & & \ddots & & \ddots & \\ & & & & & & & \ddots \end{bmatrix}.$$

Figure 6.1 contains *Ince-Strutt diagrams* [8] that depict  $\tau$  (corresponding to the critical forcing amplitude) plotted against the spatial wavenumber  $k$  for two values of the frequency  $\omega = 500$  and  $1000 \text{ s}^{-1}$ . Each point on the diagram represents a periodic solution to the linearized IB equations so that when taken together these points trace out the marginal stability contours that divide parameter space into regions corresponding to stable or unstable solutions. The contours have a characteristic “tongue-” or “finger-like” shape and alternate between harmonic and subharmonic

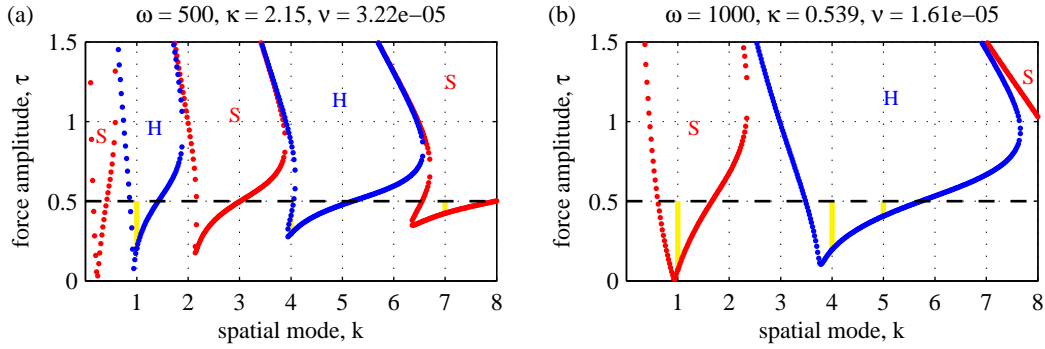


FIG. 6.1. *Ince-Strutt diagrams showing the critical forcing amplitude  $\tau$  for  $\alpha = 0$  plotted against spatial wavenumber when  $\omega = 500 \text{ s}^{-1}$  (left) and  $\omega = 1000 \text{ s}^{-1}$  (right). The physically relevant parameters for instability are highlighted by the vertical solid lines.*

solutions, labelled “H” and “S” respectively. Unstable solutions correspond to parameter values that lie above and inside each tongue, while parameter values below the tongues yield stable solutions. Although we can expect parametric resonance to occur for any choice of parameters located inside one of the unstable tongues, the parameters are further constrained by the following two physical considerations: first, that only modes corresponding to integer values of  $k$  are physically realizable; and second, that the forcing amplitude must satisfy  $\tau \leq \frac{1}{2}$  so that the BM stiffness  $K(s, t)$  remains non-negative. To get a clearer idea of the unstable modes that correspond to physical BM oscillations, we fix  $k$  at integer values ranging from 1 through 6 and display in Figure 6.2 the stability plots as a function of frequency  $\omega$  on the horizontal axis. In each case the right-most tongue is labelled “H” or “S” and the subsequent tongues moving to the left alternate between harmonic and subharmonic modes. We observe that as  $k$  increases, the contours tend to widen and shift downward and to the right; consequently, it is higher frequency modes that are more susceptible to resonant instabilities. Indeed, the lowest wavenumber modes can be excited at very low values of the forcing amplitude  $\tau$  provided the forcing frequency is high enough.

To verify the existence of these resonant solutions from our linear analysis in the case  $\alpha = 0$ , we next perform numerical simulations of the full governing IB equations (2.1)–(2.5), that now include nonlinearities from both the advection terms and the delta function integral terms. We use a standard approach similar to the algorithm described in [46], in which the fluid variables are discretized on an equally-spaced rectangular grid and the membrane on a moving set of Lagrangian points. A split-step projection method is used to solve the incompressible Navier-Stokes equations and a regularized delta function is used to approximate the integral terms that encapsulate the fluid-structure interaction. We use the IB algorithm implemented in the freely-available Matlab software package `MatIB` whose implementation details can be found in [15].

Simulations are performed on a doubly-periodic fluid domain of size  $[-L, L] \times [-L, L]$  and we use the forcing parameters  $\omega = 900, 1000, 1100 \text{ s}^{-1}$  and  $\tau = 0.1, 0.2$ , with all other parameters listed in Table 5.1. Figure 6.3 depicts the time evolution of the peak BM amplitude for an initial membrane displacement corresponding to a  $k = 1$  cosine wave with amplitude  $10^{-6} \text{ cm}$ . For the parameter values chosen, the results exhibit a range of behaviour including stable (non-resonant) solutions in which the amplitude decays over time, as well as resonant solutions that experience growth in amplitude by up to two orders of magnitude for the largest values of forcing frequency  $\omega$  and amplitude  $\tau$ . The Ince-Strutt diagram corresponding to  $k = 1$  from Figure 6.2 may be used to predict the solution stability in these simulations, and the expected solution behaviour is summarized in Table 6.1 for the parameter values corresponding to the simulations. Clearly, the linear analysis matches the stability behaviour observed in simulations. Most notably, for the case of amplitude  $\tau = 0.1$  we capture for increasing  $\omega$  how the  $k = 1$  mode transitions from stable, through the marginal stability boundary into an unstable tongue, and then returns again to the stable region.

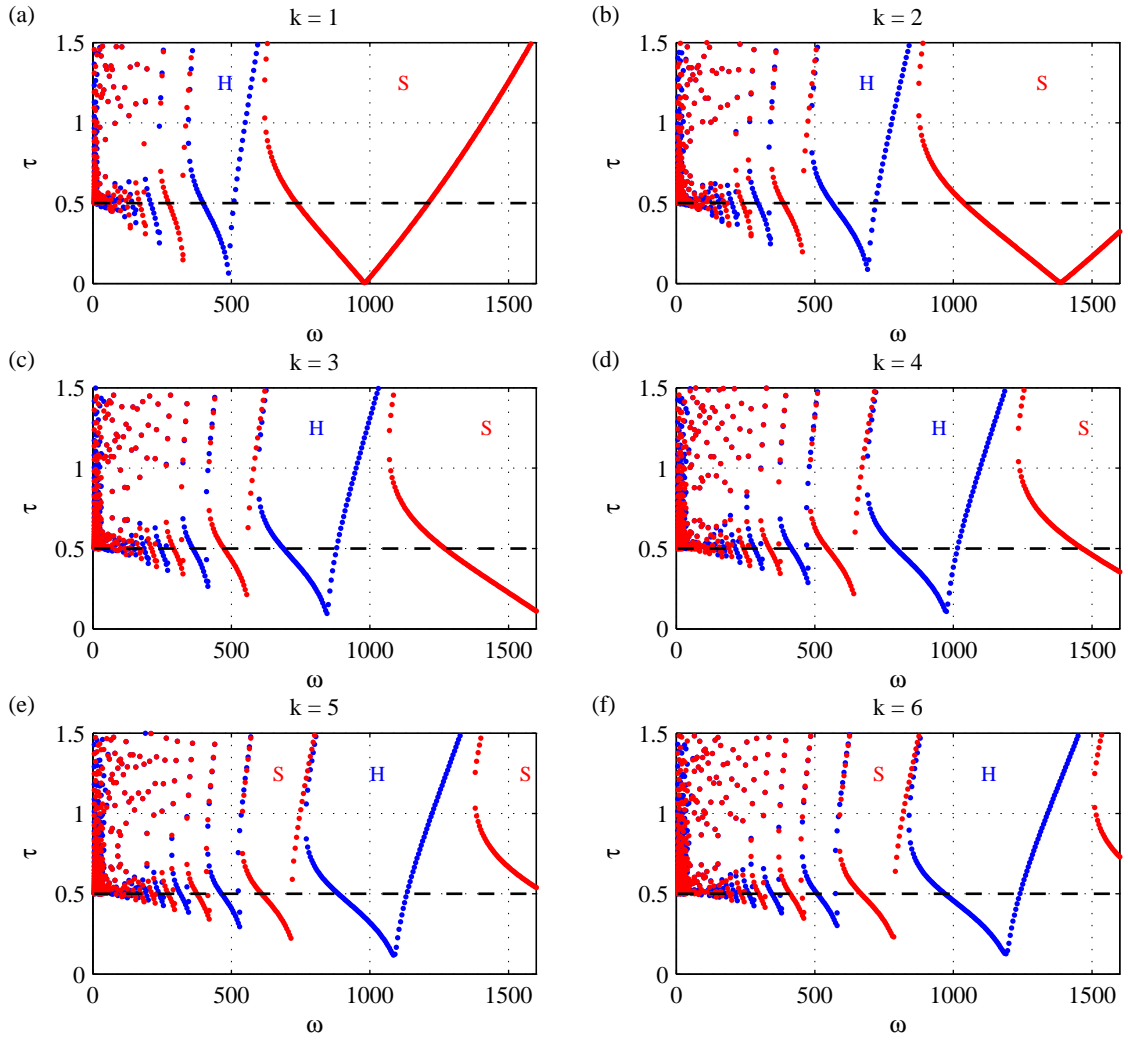


FIG. 6.2. Ince-Strutt diagrams showing the critical forcing amplitude  $\tau$  for  $\alpha = 0$  plotted against forcing frequency when  $k$  varies from 1 to 6.

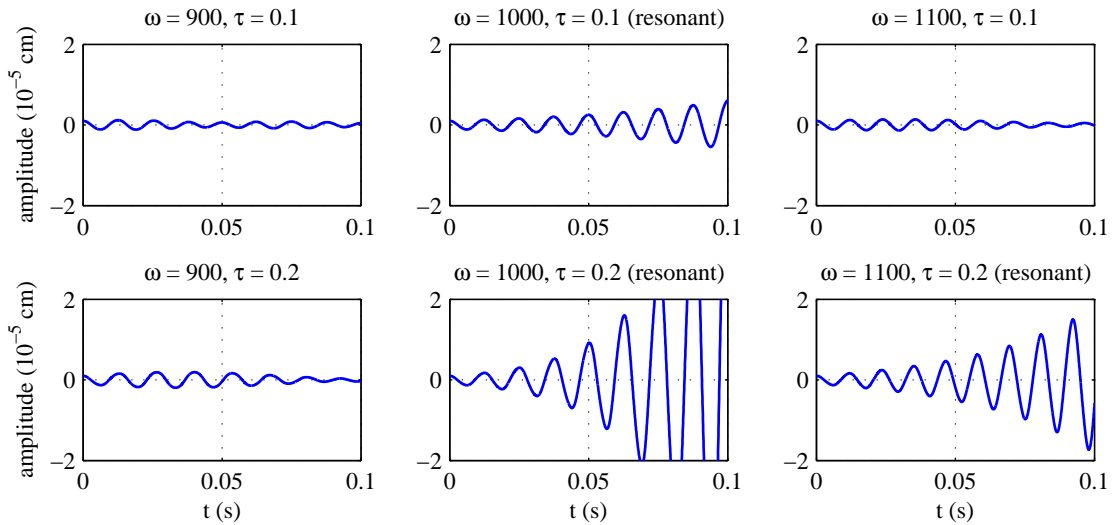


FIG. 6.3. Time evolution of the IB peak amplitude when  $\alpha = 0$  given an initial  $k = 1$  mode cosine wave profile, for various values of parameters  $\omega$  and  $\tau$ .

TABLE 6.1

Analytical stability behaviour predicted for the parameters used in Figure 6.3 with  $\alpha = 0$ .

	$\omega = 900 \text{ s}^{-1}$	$\omega = 1000 \text{ s}^{-1}$	$\omega = 1100 \text{ s}^{-1}$
$\tau = 0.1$	stable	unstable	stable
$\tau = 0.2$	stable	unstable	unstable

**6.2. Case  $\alpha \neq 0$ .** We next investigate the stability of solutions in the spatially-coupled case ( $\alpha \neq 0$ ) where the BM stiffness varies exponentially along its length. The stability contours are shown as plots of  $\tau$  versus  $\omega$  in Figure 6.4 using the same parameters listed in Table 5.1. Here we have displayed the harmonic and subharmonic mode plots separately, and we also present two sets of results that truncate the series solutions at different numbers of spatial modes,  $M = 5, 10$  and  $250$  (in all cases using  $N = 20$  temporal modes). In contrast with the  $\alpha = 0$  results from the previous section where stability contours are disjoint and the behaviour of a given mode is easy to identify, we observe that contours overlap due to the coupling between spatial modes. A similar “mode-mixing” effect has been observed in other physical systems such as the double pendulum [22]. Furthermore, we find that the number of stability contours depends strongly on the number of spatial modes  $M$  included in the truncated series expansion; in particular, increasing  $M$  gives rise to more stability contours that tend to pack more closely together. As  $M$  gets large, the contour “tongue-tips” sweep out a smooth curve that divides parameter space into stable and unstable solutions as seen in the bottom row of plots in Figure 6.4 for  $M = 250$ . We note that convergence in the time modes is much faster than in the spatial modes, thereby requiring that  $M$  be taken significantly larger than  $N$  in order to achieve accurate results. We note in particular that when either  $k > 250$  or  $n > 20$ , all coefficients satisfy  $|h_k^n| < 10^{-4}$  and so the neglected modes have negligible effect on our computed results.

Although it is no longer possible to predict the growth or decay of a single wavenumber mode as in the  $\alpha = 0$  case, we can nevertheless still identify the region in parameter space corresponding to stable solutions. Figures 6.4e and 6.4f show that for each forcing frequency there is a value of  $\tau_o$  in the interval  $[0, \frac{1}{2}]$  for which a forcing amplitude  $0 < \tau < \tau_o$  yields a stable solution whereas amplitudes  $\tau_o < \tau < \frac{1}{2}$  lead to resonance. Again, viscosity acts as a stabilizing mechanism in the sense that increasing  $\mu$  will increase  $\tau_o$  and consequently increase the size of the region in parameter space where solutions are stable. Varying  $\sigma$  has the effect of changing the range of resonant frequencies: increasing  $\sigma$  causes the contours to spread out, thereby increase the range of frequencies that result in unstable solutions.

Once again, we use numerical simulations of the full IB model equations on the domain  $\Omega = [-L, L] \times [-L, L]$  to validate the existence of resonant modes found analytically. For the initial membrane configuration, we use the same cosine wave with amplitude  $10^{-6}$  cm and wavenumber  $k = 1$ . Figures 6.5, 6.6 and 6.7 display the time variation of the amplitude of the first three Fourier cosine modes with forcing frequencies  $\omega = 400, 600$  and  $800 \text{ s}^{-1}$  respectively. In each case we also choose three different values of the forcing amplitude,  $\tau = 0.05, 0.08$  and  $0.1$ . Even though the initial condition contains a pure wavenumber  $k = 1$  mode, all  $k$ -modes are eventually excited because of the mode-coupling that arises through the spatially-dependent stiffness. According to Figure 6.4, we expect the  $\tau = 0.05$  cases to be stable (since the tips of all tongues lie above this value of  $\tau$ ) while taking  $\tau$  any larger should destabilize the solution. Indeed, numerical simulations with  $\tau = 0.05$  do show that BM oscillations decay in time and that the parametric forcing is insufficient to initiate an instability. Furthermore, when  $\tau$  is increased to  $0.08$ , the solutions become unstable, sustained oscillations appear, and for the largest value of  $\tau = 0.1$  the peak amplitude grows even larger. It is important to note that in all of the resonant cases simulated, the oscillation frequency is half of the internal forcing frequency, which is a common signature of parametric resonance.

Slight differences arise from the fact that our numerical simulations are on a doubly-periodic domain of finite length, whereas the analysis assumes a fluid domain of infinite extent in  $y$ . Although we have chosen the domain size to be large enough that boundary effects are kept to a minimum, there are still interactions between periodic BM copies that cannot be completely eliminated in our simulations.



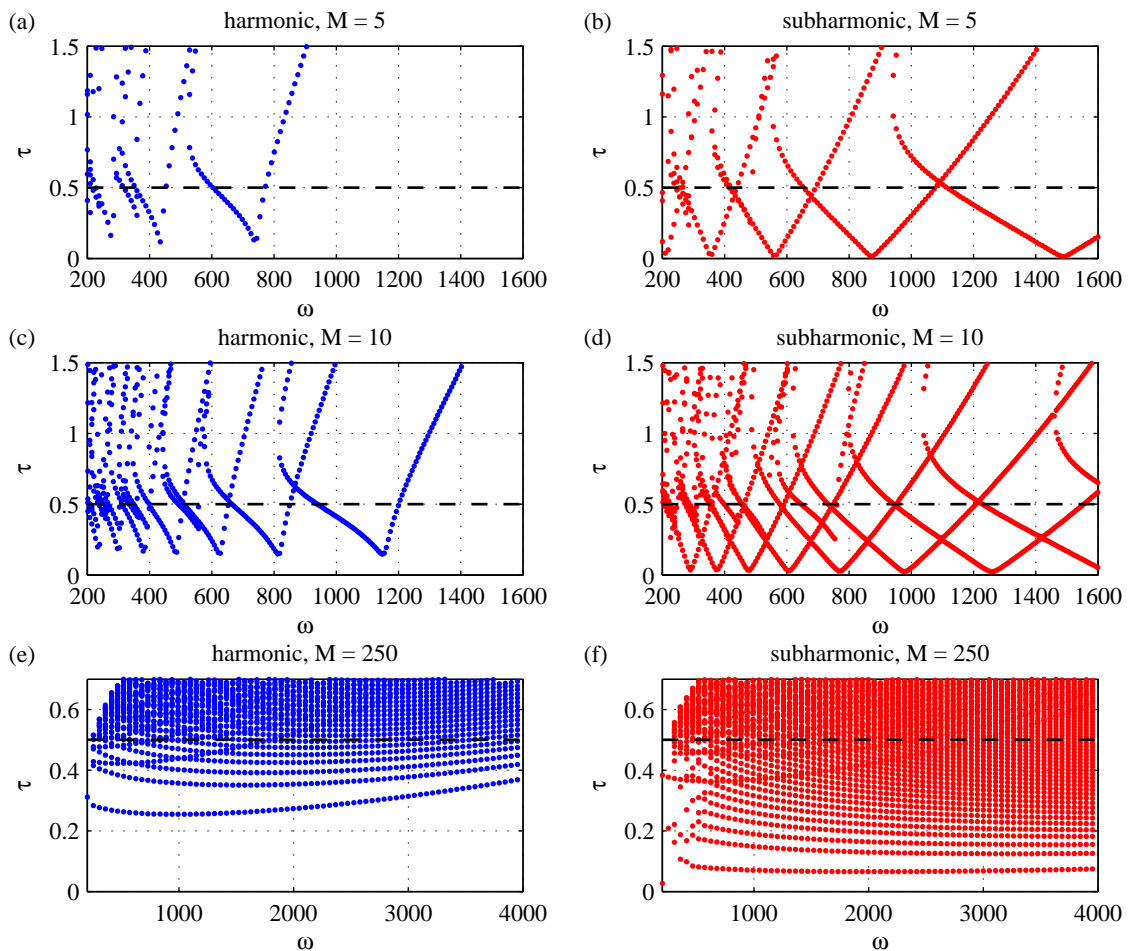


FIG. 6.4. *Ince-Strutt diagrams* for the case  $\alpha \neq 0$ , depicting the convergence of the critical forcing amplitude as the number of spatial modes  $M$  is increased from 5 (top) to 10 (middle) to 250 (bottom). The eigenvalues are separated into harmonic (left) and subharmonic (right) modes. Note the different axes for the  $M = 250$  case.

We conclude by discussing the existence of parametric resonances in our cochlea model for the full range of physically-relevant BM parameters (namely,  $\sigma$ ). Figure 6.8 displays contours of the smallest  $\tau$  resulting in resonance predicted by our analysis using  $N = 20$ ,  $M = 250$  for a human cochlea (left) and a gerbil cochlea (right). The parameters for the human cochlea are taken from Table 5.1 except for the membrane stiffness. Experimental values for  $\sigma$  reported in the literature for human cochleas exhibit a large variation, ranging from  $\sigma = 1 \times 10^7 \text{ g cm}^{-2} \text{ s}^{-2}$  from [29] to as high as  $2 \times 10^9 \text{ g cm}^{-2} \text{ s}^{-2}$  in other two-dimensional models (see [40, Table 1], for example). We consider this entire range on the vertical axis of Figure 6.8, while the horizontal axis extent covers to the the entire range of audible frequencies  $\omega \in [50, 20000] \text{ Hz}$  for humans. Stiffness values for the gerbil cochlea were extracted from [43, Fig. 8] where several experiments are summarized and show  $\sigma \in [1.5 \times 10^8, 2.0 \times 10^9] \text{ g cm}^{-2} \text{ s}^{-2}$  (a wider range is plotted). The stiffness decay parameter for the gerbil BM is estimated to be  $\lambda = 3.7 \text{ cm}^{-1}$  and the length is  $L = 1.3 \text{ cm}$  [38]. The horizontal axis of the right plot covers the audible range for a gerbil  $\omega \in [100, 50000] \text{ Hz}$ . From these plots, we observe that parametric resonance is possible ( $\tau < \frac{1}{2}$ ) for nearly all parameter values corresponding to the human cochlea, except at the highest frequencies and the lowest values of  $\sigma$ . Therefore, we can conclude that parametric resonance arising from fluid-structure interaction effects is possible in our cochlea model for most sounds in the human audible range. A similar conclusion can be drawn for the gerbil cochlea. A possible experiment to further explore these parameter ranges is to study BM response to in vitro electrical stimulation of the cochlea [9, 39] wherein electrically evoked otoacoustic emissions could be modeled as a parametric forcing in the outer hair cells.

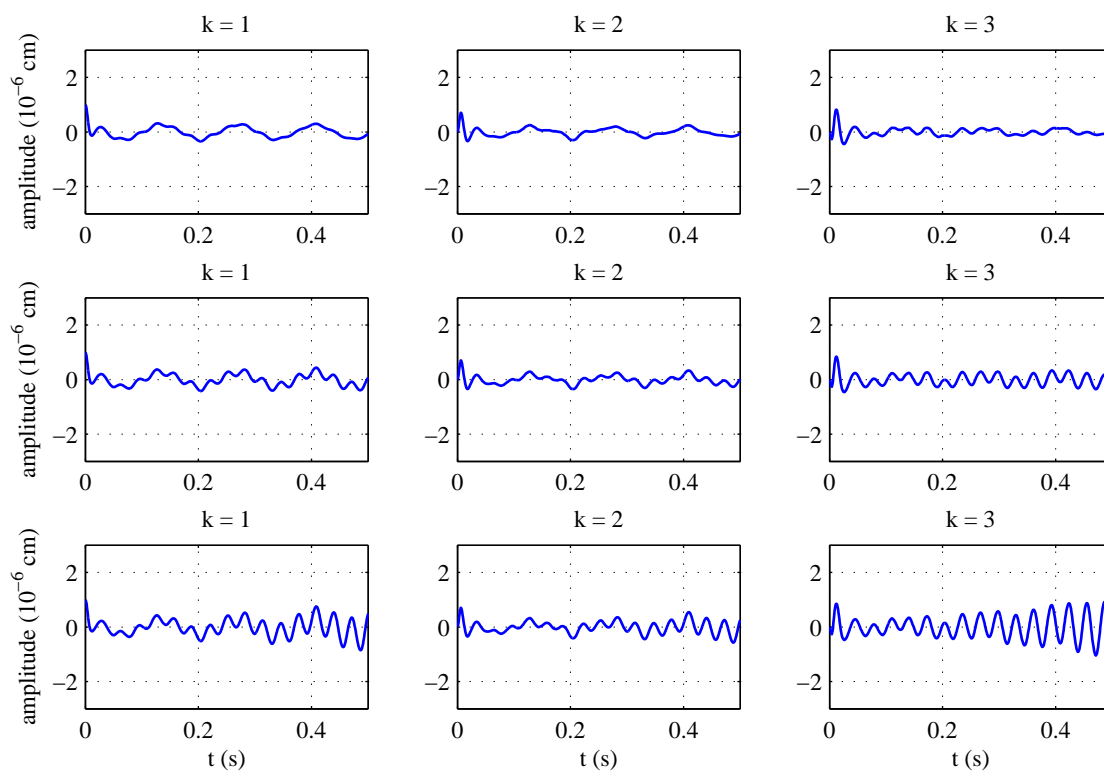


FIG. 6.5. Time evolution of the amplitude of Fourier cosine coefficients from numerical simulations for internal forcing frequency  $\omega = 400 \text{ s}^{-1}$  and stiffness forcing amplitude  $\tau = 0.05, 0.08$  and  $0.1$  (top, middle, bottom).

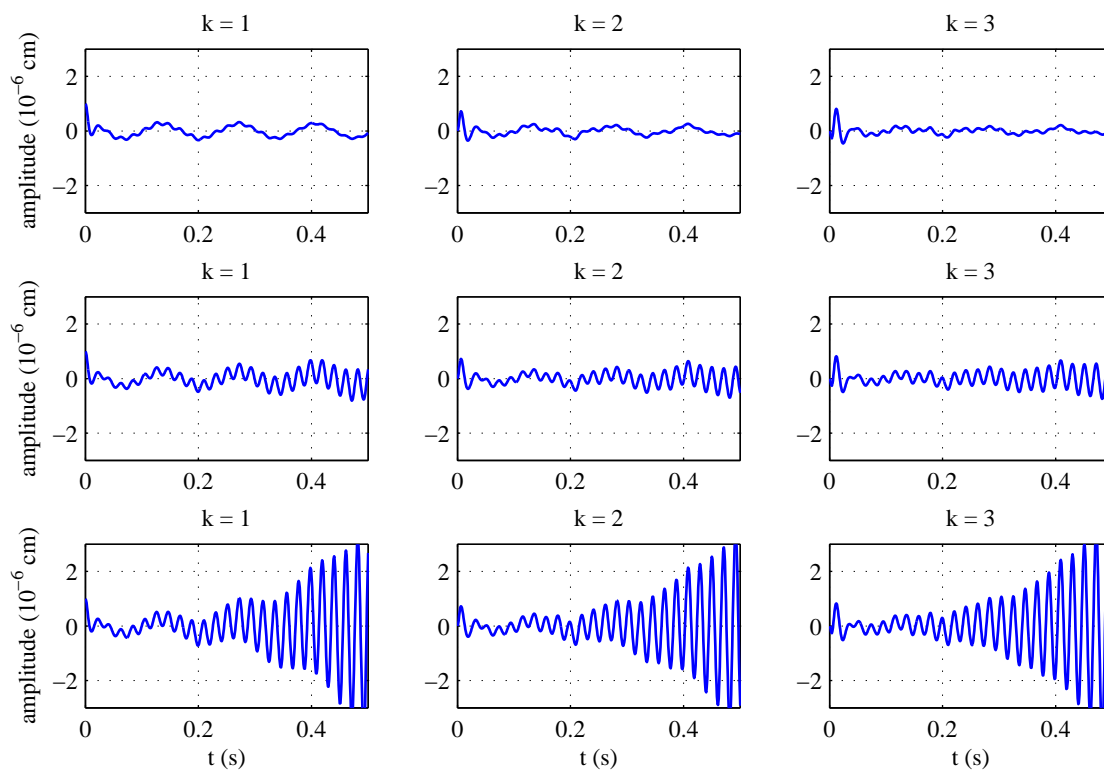


FIG. 6.6. Time evolution of the amplitude of Fourier cosine coefficients from numerical simulations for internal forcing frequency  $\omega = 600 \text{ s}^{-1}$  and stiffness forcing amplitude  $\tau = 0.05, 0.08$  and  $0.1$  (top, middle, bottom).

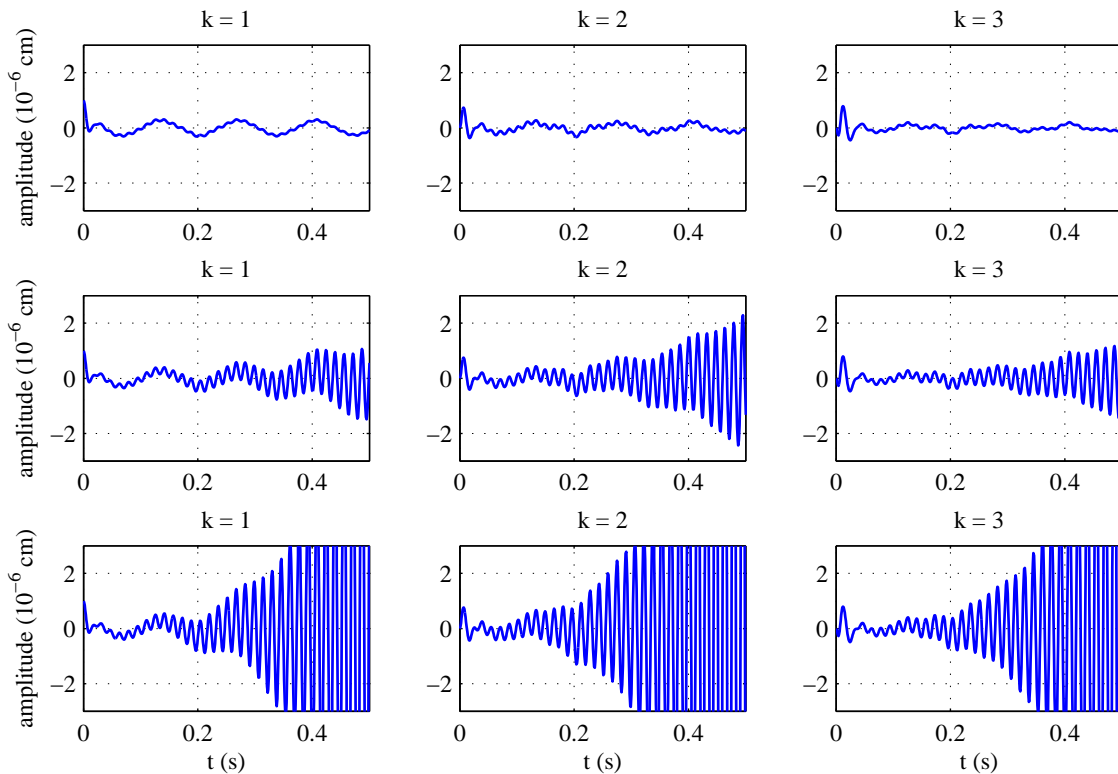


FIG. 6.7. Time evolution of the amplitude of Fourier cosine coefficients from numerical simulations for internal forcing frequency  $\omega = 800 \text{ s}^{-1}$  and stiffness forcing amplitude  $\tau = 0.05, 0.08$  and  $0.1$  (top, middle, bottom).

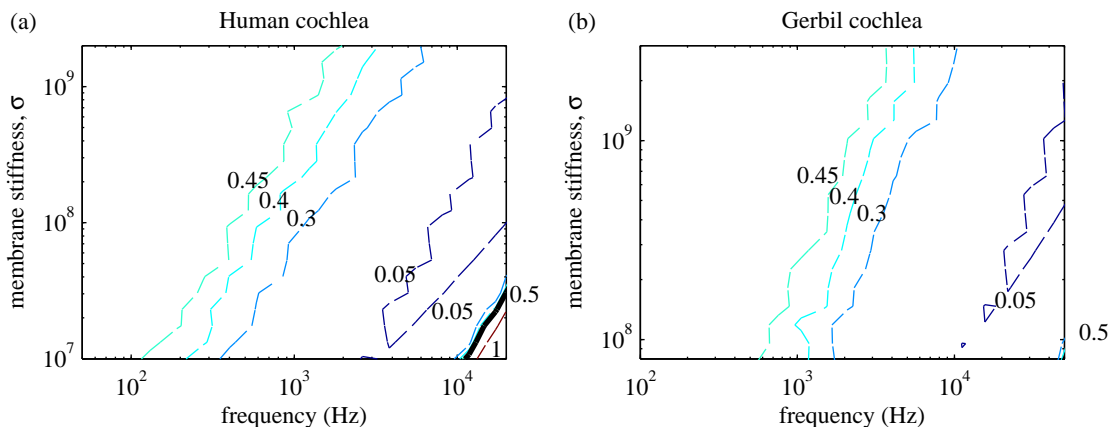


FIG. 6.8. Contour plots of minimum  $\tau$  required for parametric resonance with physically relevant parameters for the human cochlea (left) and the gerbil cochlea (right). The contour corresponding to  $\tau_o = 0.5$  is shown as a solid curve, and so only those parameters lying in the lower right corner of the diagram (small stiffness, large frequency) correspond to stable or non-resonant solutions.

**7. Summary and Conclusions.** A immersed boundary model was developed for the basilar membrane in the cochlea, for the purpose of investigating the relevance of parametric resonance as a novel mechanism for amplification of BM oscillations. Our model captures the fluid-structure interaction that occurs between the basilar membrane and the surrounding cochlear fluid. Our work is based upon a previous model from [31], but includes the additional effects of internal (parametric) forcing due to variations in the elastic properties of the BM. The prime motivation for introducing such a parametric forcing derives from the work of Mammano and Ashmore [32] who have uncovered experimental evidence that oscillations of the outer hair cells embedded in the

CP can lead to periodic modulation of the BM elastic stiffness.

We demonstrated first that a parametrically-forced membrane can produce travelling wave solutions that are similar to those observed in [31] for a passive BM. A Floquet stability analysis was then used to demonstrate the existence of resonant solutions in the linearized IB equations. The results were presented as plots of the marginal stability contours in  $\tau$ - $\omega$  (forcing amplitude-frequency) parameter space. For a spatially homogeneous membrane with a constant value of stiffness, the stability contours in the corresponding Ince-Strutt diagram are disjoint for each Fourier mode. However, for the realistic case of a BM stiffness that varies exponentially along its length, there is a mode-mixing effect in which the stability contours overlap in parameter space. We conclude that internal forcing through via the BM stiffness at sufficiently large amplitudes can induce parametric instability for any frequency in the physiological range of human hearing. The existence of these resonances is verified using numerical simulations of a full two-dimensional immersed boundary model of the cochlea.

Our main conclusion is that parametric resonances arising from fluid-structure interactions in the cochlea are worthy of further study as a possible contributing factor in the sound amplification ability of human and other mammalian hearing systems. One obvious focus for future research is to develop a more complete cochlea model that couples the fluid-structure interaction effects (giving rise to parametric resonance) along with an existing model for BM mechanical amplification [33, 35, 40, 48, 49], which would thereby permit a comparison of the relative importance of the combined effects. This would also permit us to replace the BM stiffness parameter (2.4) with a more physiologically relevant (non-separable) function in which the spatial dependence is determined by an existing mechanical model that has been validated against experiments. Our immersed boundary model is also an ideal framework to investigate effects such as longitudinal coupling within the BM [2, 26, 37] or bending-resistant stiffness that some studies claim are important [2, 47]. Finally, the active process in the cochlea has been connected by some authors with *spontaneous otoacoustic emissions* [35] for which a study of the potential impact of parametric resonance on amplifying such spontaneous oscillations would be a fascinating topic for future investigation.

**Acknowledgments.** We would like to express our thanks to Brittany Froese and Jeffrey Wiens for the use of their two-dimensional immersed boundary code MatIB [15].

#### REFERENCES

- [1] J. B. ALLEN, *Two-dimensional cochlea fluid model: New results*, J. Acoust. Soc. Am., 61 (1977), pp. 110–119.
- [2] J. B. ALLEN AND M. M. SONDEHI, *Cochlear macromechanics: Time domain solutions*, J. Acoust. Soc. Am., 66 (1979), pp. 123–132.
- [3] J. ASHMORE ET AL., *Editorial: The remarkable cochlear amplifier*, Hearing Res., 266 (2010), pp. 1–17.
- [4] R. P. BEYER, JR., *A computational model of the cochlea using the immersed boundary method*, J. Comput. Phys., 98 (1992), pp. 145–162.
- [5] R. N. BRACEWELL, *The Fourier Transform and Its Applications*, McGraw-Hill, 2000.
- [6] W. E. BROWNELL, C. R. BADER, D. BERTRAND, AND Y. DE RIBAUPIERRE, *Evoked mechanical responses of isolated cochlear outer hair cells*, Science, 227 (1985), pp. 194–196.
- [7] R. S. CHADWICK, A. INSELBERG, AND K. JOHNSON, *Mathematical model of the cochlea. II: Results and conclusions*, SIAM J. Appl. Math., 30 (1976), pp. 164–179.
- [8] A. R. CHAMPNEYS, *The dynamics of parametric excitation*, in Encyclopedia of Complexity and Systems Science, R. A. Meyers, ed., Springer, 2009, pp. 183–204.
- [9] D. CHAN AND A. J. HUDSPETH, *Mechanical responses of the organ of corti to acoustic and electrical stimulation in vitro*, Biophys. J., 89 (2005), pp. 4382–4395.
- [10] R. CORTEZ, C. S. PESKIN, J. M. STOCKIE, AND D. VARELA, *Parametric resonance in immersed elastic boundaries*, SIAM J. Appl. Math., 65 (2004), pp. 494–520.
- [11] P. DALLOS, *The active cochlea*, J. Neurosci., 12 (1992), pp. 4575–4585.
- [12] E. DE BOER, *The “inverse problem” solved for a three-dimensional model of the cochlea. I. Analysis*, J. Acoust. Soc. Am., 98 (1995), pp. 896–903.
- [13] E. DE BOER AND A. L. NUTTALL, *Cochlear mechanics, tuning, non-linearities*, in The Ear, Paul A. Fuchs, ed., vol. 1 of The Oxford Handbook of Auditory Science, Oxford University Press, 2010, ch. 5, pp. 139–177.
- [14] B. EPP, J. L. VERHEY, AND M. MAUERMANN, *Modeling cochlear dynamics: Interrelation between cochlea mechanics and psychoacoustics*, J. Acoust. Soc. Am., 128 (2010), pp. 1870–1883.
- [15] B. D. FROESE AND J. K. WIENS, *MatIB’s User Guide*, July 2013. Available at <http://github.com/eldila/MatIB>.

- [16] C. D. GEISLER, *From Sound to Synapse: Physiology of the Mammalian Ear*, Oxford University Press, New York, 1998.
- [17] E. GIVELBERG AND J. BUNN, *A comprehensive three-dimensional model of the cochlea*, J. Comput. Phys., 191 (2003), pp. 377–391.
- [18] J. HOWARD AND A. J. HUDSPETH, *Compliance of the hair bundle associated with gating of mechano-electrical transduction channels in the bullfrog's saccular hair cell*, Neuron, 1 (1988), pp. 189–199.
- [19] A. J. HUDSPETH, *Mechanical amplification of stimuli by hair cells*, Curr. Opin. Neurobiol., 7 (1997), pp. 480–486.
- [20] ———, *Making an effort to listen: Mechanical amplification in the ear*, Neuron, 59 (2008), pp. 530–545.
- [21] A. INSELBERG AND R. S. CHADWICK, *Mathematical model of the cochlea. I: Formulation and solution*, SIAM J. Appl. Math., 30 (1976), pp. 149–163.
- [22] P. JÄCKEL AND T. MULLIN, *A numerical and experimental study of codimension-2 points in a parametrically excited double pendulum*, Proc. Roy. Soc. A, 454 (1998), pp. 3257–3274.
- [23] K. D. KARAVITAKI AND D. C. MOUNTAIN, *Evidence for outer hair cell driven oscillatory fluid flow in the tunnel of Corti*, Biophys. J., 92 (2007), pp. 3284–3293.
- [24] J. B. KELLER AND J. C. NEU, *Asymptotic analysis of a viscous cochlear model*, J. Acoust. Soc. Am., 77 (1985), pp. 2107–2110.
- [25] A. KERN, C. HEID, W.-H. STEEB, N. STOOP, AND R. STOOP, *Biophysical parameters modification could overcome essential hearing gaps*, PLoS Comp. Biol., 4 (2008), p. e1000161.
- [26] Y. KIM AND J. XIN, *A two-dimensional nonlinear nonlocal feed-forward cochlear model and time domain computation of multitone interactions*, Multiscale Model. Simul., 4 (2005), pp. 664–690.
- [27] W. KO AND J. M. STOCKIE, *Correction to “Parametric resonance in immersed elastic boundaries”* (SIAM J. Appl. Math. 65(2):494–520, 2004), July 2012. arXiv:1207.4744v1 [math.AP].
- [28] M.-C. LAI AND Z. LI, *A remark on jump conditions for the three-dimensional Navier-Stokes equations involving an immersed moving membrane*, Appl. Math. Lett., 14 (2001), pp. 149–154.
- [29] M. B. LESSER AND D. A. BERKLEY, *Fluid mechanics of the cochlea: Part I*, J. Fluid Mech., 51 (1972), pp. 497–512.
- [30] R. J. LEVEQUE, C. S. PESKIN, AND P. D. LAX, *Solution of a two-dimensional cochlea model using transform techniques*, SIAM J. Appl. Math., 45 (1985), pp. 450–464.
- [31] ———, *Solution of a two-dimensional cochlea model with fluid viscosity*, SIAM J. Appl. Math., 48 (1988), pp. 191–213.
- [32] F. MAMMANO AND J. F. ASHMORE, *Reverse transduction measured in the isolated cochlea by laser Michelson interferometry*, Nature, 365 (1993), pp. 838–841.
- [33] F. MAMMANO AND R. NOBILI, *Biophysics of the cochlea: Linear approximation*, J. Acoust. Soc. Am., 93 (1993), pp. 3320–3332.
- [34] D. MANOUSSAKI, E. K. DIMITRIADIS, AND R. S. CHADWICK, *Cochlea's graded curvature effect on low frequency waves*, Phys. Rev. Lett., 93 (2006), pp. 3320–3332.
- [35] V. S. MARKIN AND A. J. HUDSPETH, *Modeling the active process of the cochlea: Phase relations, amplification, and spontaneous oscillation*, Biophys. J., 69 (1995), pp. 138–147.
- [36] P. MARTIN AND A. J. HUDSPETH, *Active hair-bundle movements can amplify a hair cell's response to oscillatory mechanical stimuli*, P. Natl. Acad. Sci., 96 (1999), pp. 14306–14311.
- [37] R. C. NAIDU AND D. C. MOUNTAIN, *Longitudinal coupling in the basilar membrane*, J. Assoc. Res. Otolaryngol., 2 (2001), pp. 257–267.
- [38] ———, *Basilar membrane tension calculations for the gerbil cochlea*, J. Acoust. Soc. Am., 121 (2007), pp. 994–1002.
- [39] H. H. NAKAJIMA, E. S. OLSON, D. C. MOUNTAIN AND A. E. HUBBARD, *Electrically evoked otoacoustic emissions from the apical turns of the gerbil cochlea*, J. Acoust. Soc. Am., 96 (1994), pp. 786–794.
- [40] S. T. NEELY, *Finite difference solution of a two-dimensional mathematical model of the cochlea*, J. Acoust. Soc. Am., 69 (1981), pp. 1386–1393.
- [41] K. E. NILSEN AND I. J. RUSSELL, *Timing of cochlear feedback: spatial and temporal representation of a tone across the basilar membrane*, Nature Neurosci., 2 (1999), pp. 642–648.
- [42] R. NOBILI, F. MAMMANO, AND J. ASHMORE, *How well do we understand the cochlea?*, Trends Neurosci., 21 (1998), pp. 159–167.
- [43] E. S. OLSON, H. DUIFHUIS, AND C. R. STEELE, *Von Békésy and cochlear mechanics*, Hearing Res., 293 (2012), pp. 31–43.
- [44] C. S. PESKIN, *Partial Differential Equations in Biology (Lecture Notes)*, Courant Institute of Mathematical Sciences, New York University, New York, 1975.
- [45] ———, *Numerical analysis of blood flow in the heart*, J. Comput. Phys., 25 (1977), pp. 220–252.
- [46] ———, *The immersed boundary method*, Acta Numer., 11 (2002), pp. 1–39.
- [47] C. POZRIKIDIS, *Boundary-integral modeling of cochlear hydrodynamics*, J. Fluid Struct., 24 (2008), pp. 336–365.
- [48] S. RAMAMOORTHY, N. V. DEO, AND K. GROSH, *A mechano-electro-acoustical model for the cochlea: Response to acoustic stimuli*, J. Acoust. Soc. Am., 121 (2007), pp. 2758–2773.
- [49] T. REICHENBACH AND A. J. HUDSPETH, *A ratchet mechanism for amplification in low-frequency mammalian hearing*, Proc. Natl. Acad. Sci. USA, 107 (2010), pp. 4973–4978.
- [50] T. REICHENBACH AND A. J. HUDSPETH, *The physics of hearing: Fluid mechanics and the active process of the inner ear*, 77 (2014), p. 076601.
- [51] C. A. SHERA, A. TUBIS, AND C. L. TALMADGE, *Coherent reflection in a two-dimensional cochlea: Short-wave versus long-wave scattering in the generation of reflection-source otoacoustic emissions*, J. Acoust. Sci. Am., 118 (2005), pp. 287–313.
- [52] J. M. STOCKIE AND B. R. WETTON, *Stability analysis for the immersed fiber problem*, SIAM J. Appl. Math.,

- 55 (1995), pp. 1577–1591.
- [53] S. VERHULST, T. DAU, AND C. A. SHERA, *Nonlinear time-domain cochlear model for transient stimulation and human otoacoustic emission*, J. Acoust. Soc. Am., 132 (2012), pp. 3842–3848.
- [54] G. VON BÉKÉSY, *Experiments in Hearing*, McGraw-Hill Book Company, New York, 1960.
- [55] J. XIN, *Dispersive instability and its minimization in time-domain computation of steady-state responses of cochlear models*, J. Acoust. Sci. Am., 115 (2004), pp. 2173–2177.
- [56] G. ZWEIG, *Finding the impedance of the organ of Corti*, J. Acoust. Soc. Am., 89 (1991), pp. 1229–1254.